PAPER

Multistage kinetic analysis of DMAA/MBAM polymer removal from gelcast ceramic parts using a multi-stage parallel reaction model and model-free method

Jing Li, [ID] [ab] Jindi Huang [ID] *[a] and Ruiming Yin[c]

This work aims to develop an effective method for investigating the multistage debinding kinetics and reaction mechanisms of removing N,N-dimethylacrylamide/N,N′-methylenebisacrylamide (DMAA/MBAM) polymer from gelcast ceramic parts. Thermogravimetry (TG) and pyrolysis-gas chromatography/mass spectrometry (Py-GC/MS) experiments were performed to investigate the thermal degradation characteristics and the main compounds produced during the pyrolysis of DMAA/MBAM polymer within green components. A multi-stage parallel reaction model (M-PRM) was proposed to separate the overlapping peaks in the $d\alpha/dT$ curves. The kinetic parameters (activation energy E and pre-exponential factor k_0) of each substage were calculated using model-free methods (Flynn–Wall–Ozawa, Starink, Friedman and Kissinger–Akahira–Sunose) and an activation energy variable model. In addition, the most appropriate kinetic mechanism function $f(\alpha)$ of each substage was analyzed and discussed *via* Málek's procedure and the Šesták–Berggren (SB) model. The results showed that the DMAA/MBAM polymer burnout in green components can be divided into three substages through a three-stage parallel reaction model (3-PRM). The values of E (Friedman method) for substages 1 to 3 were $E(\alpha) = 139.862 - 110.481\alpha + 156.161\alpha^2 - 88.714\alpha^3$ kJ mol^{-1}, $E(\alpha) = 160.791 + 152.496\alpha - 236.906\alpha^2 + 163.724\alpha^3$ kJ mol^{-1} and $E(\alpha) = 72.132 + 452.830\alpha - 669.039\alpha^2 + 507.015\alpha^3$ kJ mol^{-1}, respectively. The average values of E showed an increasing tendency from substages 1 to 3, and a kinetic compensation effect was also observed between the E and k_0 in each substage. The kinetic mechanism analysis revealed that the reaction mechanisms for substages 1 to 3 were $f(\alpha) = (1 - \alpha)^{0.668}\alpha^{3.049}(-\ln(1 - \alpha))^{-3.874}$, $f(\alpha) = (1 - \alpha)^{0.700}\alpha^{3.177}(-\ln(1 - \alpha))^{-3.962}$ and $f(\alpha) = (1 - \alpha)^{1.049}\alpha^{-0.161}(-\ln(1 - \alpha))^{0.518}$, respectively. It is expected that the research results can be extended to investigate the multiplex debinding of binders or polymers for various colloidal molding techniques.

1 Introduction

Gelcasting is an emerging colloidal molding technology for near-net shaping of ceramic parts.[1–3] This technique ingeniously utilizes the *in situ* polymerization of the gel system to form a three-dimensional network to enwrap and immobilize ceramic particles, allowing them to keep the desired shape of green bodies.[4] The gelcasting processing mainly consists of four steps: preparation of ceramic slurries with low viscosity and high solids content, injection of slurries into the mold, demolding and drying, and debinding and sintering. The development of a reasonable debinding process, which is a critical step in the gelcasting process, is essential for obtaining compact and defect-free sintered bodies.[5,6] At present, the main methods for removing polymer or binder are classified into four categories: catalytic debinding,[7] solvent debinding,[8,9] thermal debinding[10,11] and wicking debinding.[12] For gelcasting, the organic polymer formed by the polymerization of the monomer is insoluble in the solvent and does not melt; thus, it cannot be removed by processes such as wicking debinding and solvent debinding. The related reports mainly use the thermal debinding technique.[13–15]

Removing gel from gelcast green components is a complex process involving various physical and chemical reactions, such as the diffusion of residual moisture, the degradation reaction of the polymer, mass transfer and heat transfer in porous media and evolution of stress and strain,[16,17] as shown in Fig. 1. If the gel is not completely removed, then the polymeric residues will be passed to the next process, influencing the final properties of the sintered bodies. If the gel is removed too quickly, defects

[a]School of Energy and Mechanical Engineering, Jiangxi University of Science and Technology, Nanchang, 330013, P. R. China. E-mail: hjd041@163.com

[b]School of Metallurgy and Environment, Central South University, Changsha, 410083, P. R. China

[c]College of Metallurgical Engineering, Hunan University of Technology, Zhuzhou, 412008, P. R. China
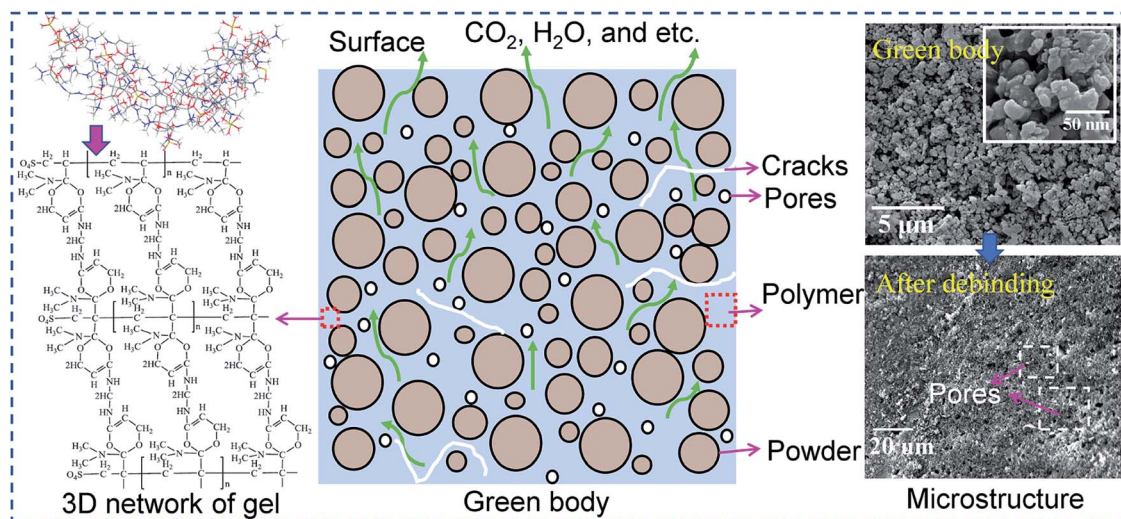
Fig. 1 Mass and heat transport processes during debinding.

such as voids and cracks may form, and these defects will also be passed to the next process, further affecting the microstructure of the ceramic parts during sintering. These effects are signs that the key to thermal debinding is successfully controlling the degradation of the polymer while ensuring complete removal without introducing defects in the green parts. Accordingly, systematic research on debinding kinetics is necessary. At present, single-step reaction models such as the Kissinger,[18] Ozawa,[18] Coats–Redfern integration[14] and model-free[19] methods have been used to estimate thermal debinding kinetic parameters such as activation energy and pre-exponential factor. However, the rate control mechanism of the binder or polymer pyrolysis during thermal debinding has not been reported. Shi et al.[17] assumed that the burnout of the polymeric binder is controlled by diffusion reactions and proposed a diffusion-controlled model for predicting the debinding kinetics of binder within powder compacts. It is known that different polymers have different thermal stabilities and may be controlled by multiple reaction mechanisms. Usually, it is difficult to accurately describe kinetic behavior with complex variations in apparent activation energy caused by changes in the reaction mechanism via a single-step reaction model.[20] Therefore, understanding the reaction mechanism and determining the limiting step of the thermal debinding process can provide a fundamental theoretical basis for obtaining more accurate kinetic parameters.

Currently, as a low-toxicity monomer, DMAA has attracted great interest for gelcasting various ceramic materials with low gel concentrations (e.g., porous Si_3N_4 ceramics,[2] ZTA composites,[21] ZrO_2,[22] SiO_2,[23] Al_2O_3,[1,24] AlN[25]); however, very limited research on its debinding behavior and reaction mechanisms has been conducted. In contrast, many investigations have concentrated on the thermal stability of DMAA/MBAM polymer through experimental thermogravimetric (TG) analysis.[21,26] In an earlier work, we developed a three-parallel-distributed activation energy model to predict debinding behavior and estimate kinetic parameters.[27] The reported theoretical predictions

of pyrolysis kinetics of DMAA/MBAM polymer agree well with experimental findings. However, explicit debinding mechanisms, which are extremely important for determining the controlling mechanisms of mass transport in the green components during the overall debinding process, have not been revealed.

The present study is intended to seek an effective method of investigating the multistage debinding kinetics and reaction mechanisms of DMAA/MBAM polymer pyrolysis in gelcast ceramic parts. The main purpose is to obtain insight into the multiple debinding mechanisms to provide useful and reliable theoretical support for the design and optimization of multistep thermal debinding technology. The thermal degradation characteristics of DMAA/MBAM polymer within green parts were investigated by thermogravimetry experiments, and the main compounds in the fast pyrolysis of DMAA/MBAM polymer were identified by pyrolysis-gas chromatography/mass spectrometry (Py-GC/MS). A multi-stage parallel reaction model (M-PRM) was proposed to analyze and separate the overlapping peaks in $d\alpha/dT$ curves. The kinetic parameters of each substage were calculated using model-free methods. In addition, the most appropriate kinetic mechanism function of each substage was analyzed and discussed via Málek's procedure and the Šesták–Berggren (SB) model.

2 Experimental methods

2.1 Raw materials

For gelcasting, a low toxicity aqueous gel system using DMAA (Kowa Co., Ltd., Japan) and MBAM (Aladdin Industrial Co., Ltd., China) as the monomer and crosslinker, respectively, was used for polymerization. Ammonium polyacrylate (NH₄PAA, Shenzhen Highrun Chemical Industry Co. Ltd., China), $(NH_4)_2S_2O_8$ (APS) and N,N,N',N'-tetramethylethylene-diamine (TEMED, Aladdin Industrial Co., Ltd., China) were used as dispersant, initiator and catalyst, respectively, according to the approach reported in our previous work.[27,28]

Y-α-SiAlON, with a composition of $Y_{0.5}Si_{9.75}Al_{2.25}O_{0.75}N_{15.25}$ ($m = 1.5$, $n = 0.75$), was selected for investigation. Additional amounts of 3 wt% Y_2O_3 and 6 wt% Ce_2O_3 were used to promote sintering densification. The raw materials were α-Si_3N_4 (SN-E10, UBE Industries, Ube, Japan), AlN ($d = 2.0$ μm, purity of 99.9%, Aladdin Industrial Co., Ltd., China), Al_2O_3 ($d = 0.5$ μm, purity of 99.9%, AKP-50, Sumitomo Chemical, Japan), Y_2O_3 (grade fine, purity of 99.9%, H.C. Stark, Germany) and Ce_2O_3 ($d = 5$ μm, purity of 99.9%, Aladdin Industrial Co., Ltd., China). To avoid the flocculation of the suspension caused by the hydrolysis reaction of AlN powder in aqueous solution, thermal oxidation treatment was used to obtain AlN with a modified surface (called M-AlN) to obtain hydrolytic resistance, following the approach reported by Li et al.[29]

2.2 Green body preparation

The gelcasting process of a green body includes the following steps. (1) The premixed solution is prepared by dissolving DMAA, MBAM (DMAA : MBAM = 16 : 1, DMAA + MBAM = 12.4 wt%) and NH$_4$PAA (1.0 wt%) in deionized water. The pH value of the premixed solution was adjusted to approximately 11 by $NH_3 \cdot H_2O$. (2) The suspensions are prepared by adding mixture powders into the premixed solution. The solid loading of the suspensions was 40 vol%. To increase the dispersion uniformity of the slurry, the Si_3N_4, Al_2O_3, Y_2O_3 and Ce_2O_3 were first added to the slurry under constant stirring and ball milled for 3 h in a planetary mill using ZrO_2 balls. The rotating rate was 255 rpm, and the weight ratio of ball-to-powder-to water was 1.9 : 1 : 0.4. Then, M-AlN was added, and the planetary mill was run without ZrO_2 balls for 30 min to prevent the wear of the dense alumina film of M-AlN flowed by degassing for 30 min. (3) The gelation process of the slurry proceeded by adding 1.0 wt% initiator and catalyst. The suspensions were cast into a cylindrical mold (∅ 35 mm × 25 mm) and then cured at room temperature until the DMAA and MBAM were fully polymerized. Then, they were demolded in a drying oven at 60 °C for 24 h. (4) The drying process is performed. The demolded wet ceramic parts were moved to a temperature and humidity test chamber and dried under controlled temperature and humidity conditions to avoid cracking and uneven shrinkage of the body due to the rapid evaporation of water. Then, the green bodies were obtained for subsequent thermal analysis.

2.3 TG analysis

The green body sample was grinded to pass through a 100-mesh sieve for the nonisothermal TG experiment. The TG analysis of the green body was performed using a thermo gravimetric analyzer (STA-449 F3 Jupiter, NETZSCH, Germany) at heating rates of 2.5, 5, 10, 15, and 20 °C min^{-1}. In the experiment, approximately 14 ± 0.5 mg of sample was placed on the crucible of the thermal analyzer. The temperature range was 35–900 °C. Pure Argon (>99.999%), and a flowrate of 40 ml min^{-1} was applied for all experiments.

2.4 Py-GC/MS analysis

The pyrolysis mechanism of the DMAA/MBAM polymer was investigated by analytical Py-GC/MS (Shimadzu QP2010 GCMS-EGA FRONTERE3030D PY). The pyrolysis temperatures were set to 240, 385 and 450 °C for 90 s; then, the pyrolysis gases were introduced into the GC/MS via a transfer line for on-line analysis. The temperature program for GC is as follows: the oven was heated from 200 °C (isothermal for 3 min) to 240 °C (isotherm for 15 min) at a heating rate of 5 °C min^{-1}; pure Ar (99.999%) was used as the carrier gas at a flow rate of 1.0 ml min^{-1}; and the split ratio was 50 : 1. The MS conditions were as follows: the ion source was EI mode (70 eV) with a temperature of 200 °C, and the mass was scanned from m/z 2 to 600 amu. The chromatographic peaks were identified based on the NIST mass spectra library.

3 Kinetic modeling

The primary purpose for investigating the pyrolysis kinetics is to obtain the multiplex debinding mechanisms of the DMAA/MBAM polymer and further to predict the entire pyrolysis process. In this study, the kinetic parameters (activation energy E and pre-exponential factor k_0) and reaction mechanisms are estimated by following various kinetic models. The flow diagram of the DMAA/MBAM polymer pyrolysis kinetic analysis is shown in Fig. 2.

3.1 Theory of kinetic triplets

The decomposition rate ($d\alpha/dt$) of the DMAA/MBAM polymer for nonisothermal reactions is expressed by the following equation:

$$\frac{d\alpha}{dt} = k(T)f(\alpha) \tag{1}$$

where $f(\alpha)$ is the differential form of the reaction mechanism function, α is the conversion of polymer during pyrolysis processes, and $k(T)$ is the Arrhenius rate constant, which are described by eqn (2) and (3), respectively.
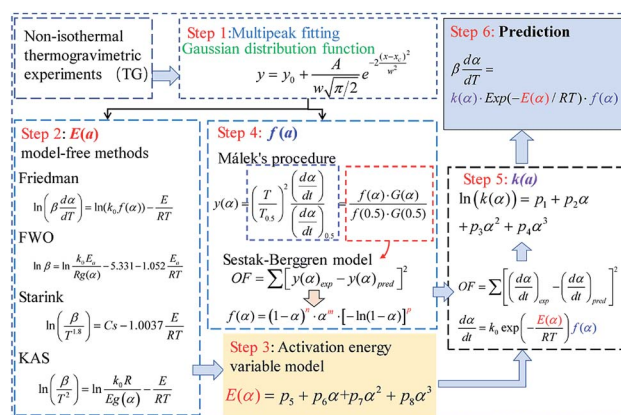

Fig. 2 The flow diagram of DMAA/MBAM polymer pyrolysis kinetic analysis.

$$\alpha = (m_0 - m_t)/(m_0 - m_\infty) \tag{2}$$

$$k(T) = k_0 \exp(-E/RT) \tag{3}$$

here, m_0, m_t, and m_∞ are the initial, actual and final masses of the gel polymer, respectively; k_0 is the pre-exponential factor; E is the apparent activation energy; R is the universal gas constant; and T is the temperature.

The nonisothermal kinetic equation can be expressed as follows:

$$\frac{d\alpha}{dT} = kf(\alpha) = \frac{k_0}{\beta} \exp\left(-\frac{E}{RT}\right)(1-\alpha)^n \tag{4}$$

$$g(\alpha) = \int_0^\alpha \frac{d\alpha}{f(\alpha)} \approx \frac{k_0}{\beta} \int_0^T \exp\left(-\frac{E}{RT}\right) dT = \frac{k_0 E}{\beta R} p(y) \tag{5}$$

$$y = E/(RT), \quad p(y) = -\int_\infty^y \frac{\exp(-y)}{y^2} dy \tag{6}$$

where β is the heating rate and $\beta = dT/dt$, n is the reaction order of the decomposition reaction of DMAA/MBAM copolymer, which is assumed to be an isothermal homogeneous reaction ($f(\alpha) = (1-\alpha)^n$), and $g(\alpha)$ is the integral form of the reaction mechanism function.

3.2 Theory of model-free methods

In thermal degradation kinetic analysis, model-free methods can be used to obtain the activation energy for any reaction progress without considering reaction mechanism.[19,30] In this study, four commonly used model-free methods, namely, the Flynn–Wall–Ozawa (FWO), Starink, Friedman and Kissinger–Akahira–Sunose (KAS) methods, are used to study the pyrolysis process of the DMAA/MBAM polymer during debinding.

The FWO method is established based on Doyle's approximation.[31] After rearranging and taking the common logarithm, Doyle's approximation equation, that is, $\ln p(y) = -5.331 - 1.052y$, is substituted into eqn (5), and the following linear relationship is obtained:

$$\ln \beta = \ln \frac{k_0 E}{R g(\alpha)} - 5.331 - 1.052 \frac{E}{RT} \tag{7}$$

where $g(\alpha) \approx \frac{k_0 E}{\beta R}\left(0.0048 \exp\left(-1.052 \frac{E}{RT}\right)\right)$.

The Starink method[32,33] is considered to have the highest accuracy, and its equation is expressed as:

$$\ln\left(\frac{\beta}{T^{1.8}}\right) = C_s - 1.0037 \frac{E}{RT} \tag{8}$$

For the same value of α of the DMAA/MBAM polymer at different heating rates, $\ln(\beta)$ is plotted vs. $1/T$ for the FWO method, and $\ln(\beta/T^{1.8})$ is plotted vs. $1/T$ for the Starink method. The values of E are estimated from the slope of the regression lines.

The KAS method uses the Coats–Redfern approximation, which is $p(y) = \exp(-y)/y^2$, therefore, eqn (5) is rearranged as

$g(\alpha) = \frac{k_0 E}{\beta R} \exp(-y/y^2)$. Then, the logarithm of both sides of the rearranged equation is taken; thus, the mathematical expression is proposed as:[34]

$$\ln\left(\frac{\beta}{T^2}\right) = \ln \frac{k_0 R}{E_a g(\alpha)} - \frac{E}{RT} \tag{9}$$

Under isoconversional conditions, $\ln(\beta/T^2)$ is plotted vs. $1/T$, and the apparent activation energy E can be determined according to the slopes of the regression lines of $-E/R$ at different heating rates.

The differential Friedman approach has recently been considered the most accurate method, and is established without approximation algorithms.[19] The equation is expressed as:

$$\ln\left(\beta \frac{d\alpha}{dT}\right) = \ln(k_0 f(\alpha)) - \frac{E}{RT} \tag{10}$$

If the regression lines of $\ln\left(\beta \frac{d\alpha}{dT}\right)$ vs. $1/T$ for the Friedman method are plotted, then the apparent activation energy E can be determined according to the slopes of the regression lines at different heating rates.

3.3 Model-fitting method

3.3.1 M-PRM. M-PRM considers the overall pyrolysis stage to be a combination of several independent reactions. Assuming that there are a series of subpeaks in the entire pyrolysis process and that each subpeak represents an independent reaction, the kinetic parameters of the entire pyrolysis stage can be considered to be the weights of the kinetic parameters of each substage. The nonisothermal pyrolysis kinetics of stage i can be described by the following differential equation:

$$d\alpha_i/dT = k_{0,i}/\beta \exp(-E_i/RT)f_i(\alpha_i) \tag{11}$$

The weighted factor of parallel reaction stage i is calculated by eqn (12):

$$w_i = (m_{i0} - m_{if})/(m_0 - m_f), \quad \sum_{i=1}^N w_i = 1 \tag{12}$$

where w_i is the weighted factor of stage i, m_0 is the initial weight, m_f is the final weight, and i is the ith stage.

Then, α and E for the overall pyrolysis reaction process can be written as:

$$\alpha = (m_0 - m_T)/(m_0 - m_f) = \sum_{i=1}^N w_i \alpha_i \tag{13}$$

$$E = \sum_{i=1}^N w_i E_i \tag{14}$$

where m_T is the mass of the gel polymer at temperature T, and N is the total number of substages.

M-PRM uses a multipeak fitting method to separate the overlapping peaks in the reaction rate ($d\alpha/dT$) or differential thermogravimetric (DTG) curve. In this study, the Gaussian distribution function eqn (15) is used to fit the $d\alpha/dT$ curve. The Levenberg–Marquardt algorithm is used for curve fitting.

$$y = y_0 + \frac{k_0}{w\sqrt{\pi/2}}e^{-2\frac{(x-x_c)^2}{w^2}} \tag{15}$$

3.3.2 Activation energy variable model. Then, the kinetic parameters (E and k_0) of each substage can be determined by model-free methods. Additionally, an activation energy variable model reported by Sun *et al.*[35] can be applied to describe the dependency between the activation energies and conversion for different substages. The theory of the activation energy variable model can be expressed as:

$$\beta\frac{d\alpha}{dT} = k(\alpha)\exp\left(-\frac{E(\alpha)}{RT}\right)f(\alpha) \tag{16}$$

where $\ln[k(\alpha)] = p_1 + p_2\alpha + p_3\alpha^2 + p_4\alpha^3$, $E(\alpha) = p_5 + p_6\alpha + p_7\alpha^2 + p_8\alpha^3$.

After taking the common logarithm, the eqn (16) can be written as:

$$\ln\left(\beta\frac{d\alpha}{dT}\right) = \ln(k(\alpha)f(\alpha)) - \frac{E(\alpha)}{RT} \tag{17}$$

$\ln\left(\beta\frac{d\alpha}{dT}\right)$ *vs.* $1/T$ can be plotted at the same fractional extent of conversion α from a series of non-isothermal thermogravimetric experiments at different heating rates. The activation energy $E(\alpha)$ can be estimated from the slope of the regression lines of $\ln\left(\beta\frac{d\alpha}{dT}\right)$ *vs.* $1/T$. On this basis, the model parameters (p_5, p_6, p_7 and p_8) can be obtained by polynomial regression fitting.

Based on the data of $f(\alpha)$, $E(\alpha)$, $d\alpha/dt$, T and α, the unknown model parameters (p_1, p_2, p_3 and p_4) can be obtained by minimizing the objective function (OF) using the generalized reduced gradient (GRG) method in Microsoft Excel Solver.[36]

$$OF = \sum\left[\left(\frac{d\alpha}{dt}\right)_{exp} - \left(\frac{d\alpha}{dt}\right)_{pred}\right]^2 \tag{18}$$

where $(d\alpha/dt)_{exp}$ and $(d\alpha/dt)_{pred}$ represent the experimental and predicted data of reaction rate ($d\alpha/dt$), respectively.

3.4 Determination of the mechanism function

3.4.1 Málek's procedure. It has been reported that Málek's procedure is an effective method for determining $f(\alpha)$ or $G(\alpha)$, which can be described as follows:[32,33]

$$y(\alpha) = \left(\frac{T}{T_{0.5}}\right)^2\frac{\left(\frac{d\alpha}{dt}\right)}{\left(\frac{d\alpha}{dt}\right)_{0.5}} = \frac{f(\alpha)G(\alpha)}{f(0.5)G(0.5)} \tag{19}$$

where $y(\alpha)$ indicates the defining function, $G(\alpha)$ is the integral form of $f(\alpha)$, and $T_{0.5}$ and $(d\alpha/dt)_{0.5}$ denote the temperature and reaction rate, respectively, when $\alpha = 0.5$.

The most appropriate kinetic mechanism function $f(\alpha)$ is deduced from the theoretical curve of $y(\alpha)$.

Arbitrarily, α_i, $y(\alpha_i)$ ($i = 1, 2, ..., j$) and $\alpha = 0.5$, $y(0.5)$ are substituted into the following equation, and the theoretical master plot $f(\alpha)G(\alpha)/f(0.5)G(0.5)$ *vs.* α can be obtained.

$$y(\alpha) = \frac{f(\alpha)G(\alpha)}{f(0.5)G(0.5)} \tag{20}$$

Substituting, α_i, T_i, $(d\alpha/dt)_i$ ($i = 1, 2, ...,j$) and $\alpha = 0.5$, $T_{0.5}$, $(d\alpha/dt)_{0.5}$ into eqn (19) provides the experimental master plot of $(T/T_{0.5})^2(d\alpha/dt)/(d\alpha/dt)_{0.5}$ *vs.* α.

$$y(\alpha) = \left(\frac{T}{T_{0.5}}\right)^2\frac{\left(\frac{d\alpha}{dt}\right)}{\left(\frac{d\alpha}{dt}\right)_{0.5}} \tag{21}$$

If the experimental plot overlaps with the theoretical plot or if the experimental data points all fall on a certain theoretical plot, then the chosen $f(\alpha)$ can be considered to be the most likely kinetic mechanism function. The common functions of the kinetic mechanism for $f(\alpha)$ and $G(\alpha)$ are summarized in Table 1.[20,33]

3.4.2 SB model. The Šesták–Berggren (SB) model has been reported as a powerful tool for the description of the reaction mechanism of single-step combined kinetics.[37] The mathematical expression can be described as:[38]

$$f(\alpha) = (1 - \alpha)^n\alpha^m[-\ln(1 - \alpha)]^p \tag{22}$$

where m, n and p refer to constant parameters. Here, the m, n and p represent the reaction order, the power law, and the diffusion mechanisms, respectively.[36,38]

Based on the data of $d\alpha/dt$, T and α, the unknown model parameters (m, n and p) can be obtained by minimizing the objective function (OF) using the generalized reduced gradient (GRG) method in Microsoft Excel Solver.[36]

$$OF = \sum[y(\alpha)_{exp} - y(\alpha)_{pred}]^2 \tag{23}$$

where $y(\alpha)_{exp}$ and $y(\alpha)_{pred}$ represent the experimental and predicted data of $y(\alpha)$, respectively.

4 Results and discussion

4.1 TG and Py-GC/MS analysis

Fig. 3 shows the TG and DTG curves of the DMAA/MBAM polymer in the gelcast green bodies obtained at 2.5, 5, 15 and 20 °C min^{-1}. As illustrated in Fig. 3, it can be seen that both TG and DTG curves show similar trends for all heating rates. From the TG curves in Fig. 3, a small mass loss is found at a temperature below 200 °C, which should correspond to the removal of residual moisture (free/bound water) absorption in the polymer.

Table 1 Expressions of the most common functions for kinetic mechanisms

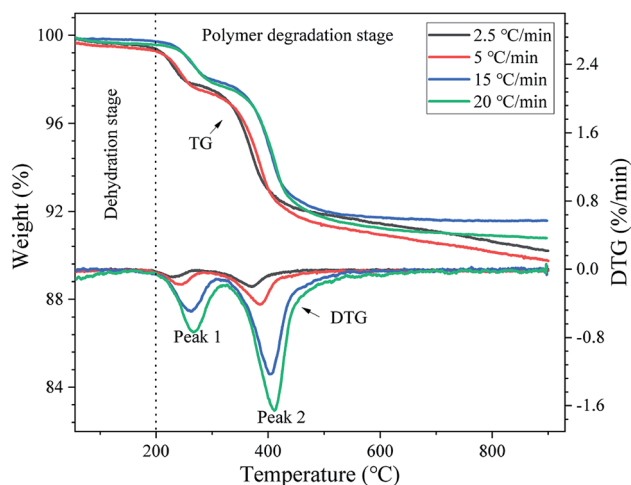| Number	Model	Differential form $f(\alpha)$	Integral form $G(\alpha)$
Diffusion models			
1	1D	$\frac{1}{2}\alpha^{-1}$	α^2
2	2D Diffusion-Valensi D-V$_2$	$[-\ln(1-\alpha)]^{-1}$	$\alpha + (1-\alpha)\ln(1-\alpha)$
3	2D Diffusion-Jander D-J$_2$	$4(1-\alpha)^{\frac{1}{2}}\left[1-(1-\alpha)^{\frac{1}{2}}\right]^{\frac{1}{2}}$	$\left[1-(1-\alpha)^{\frac{1}{2}}\right]^{\frac{1}{2}}$
4	3D Diffusion-Jander D-J$_3$	$6(1-\alpha)^{\frac{2}{3}}\left[1-(1-\alpha)^{\frac{1}{3}}\right]^{\frac{1}{2}}$	$\left[1-(1-\alpha)^{\frac{1}{3}}\right]^{\frac{1}{2}}$
5	3D Diffusion-Ginstlin–Brounshtein D-GB$_3$	$\frac{3}{2}\left[(1-\alpha)^{-\frac{1}{3}}-1\right]^{-1}$	$1-\frac{2}{3}\alpha-(1-\alpha)^{\frac{2}{3}}$
6	3D Zhuravlev–Lesokhin–Tempelman D-ZLT$_3$	$\frac{3}{2}(1-\alpha)^{\frac{4}{3}}\left[(1-\alpha)^{-\frac{1}{3}}-1\right]^{-1}$	$\left[(1-\alpha)^{-\frac{1}{3}}-1\right]^2$
Sigmoidal rate equations			
7	Avrami–Erofeev A$_3$	$3(1-\alpha)[-\ln(1-\alpha)]^{\frac{2}{3}}$	$[-\ln(1-\alpha)]^{\frac{1}{3}}$
8	Avrami–Erofeev A$_4$	$4(1-\alpha)[-\ln(1-\alpha)]^{\frac{3}{4}}$	$[-\ln(1-\alpha)]^{\frac{1}{4}}$
Reaction-order models			
9	Second-order F$_2$	$(1-\alpha)^2$	$(1-\alpha)^{-1}-1$
10	Third-order F$_3$	$(1-\alpha)^3$	$-\frac{1}{2}(1-(1-\alpha)^{-2})$
11	Fourth-order F$_4$	$(1-\alpha)^4$	$-\frac{1}{3}(1-(1-\alpha)^{-3})$
Exponent power models			
12	First-order E$_1$	α	$\ln(\alpha)$
13	Second-order E$_2$	$\frac{1}{2}\alpha$	$\ln(\alpha)^2$
Šesták–Berggren model			
14	Šesták–Berggren S–B	$(1-\alpha)^n\alpha^m[-\ln(1-\alpha)]^p$	$\int_0^\alpha \frac{d\alpha}{f(\alpha)}$

Fig. 3 TG and DTG curves of the DMAA/MBAM polymer during debinding at different heating rates.

copolymer mainly occurs in two temperature ranges: 200–300 °C and 300–600 °C. As shown in the DTG curves in Fig. 3, two strong peaks were observed and the peak maximum temperatures for DMAA/MBAM polymer degradation at heating rates of 2.5, 5, 15 and 20 °C min^{-1} are presented in Table 2. From Table 2, the maximum loss rate (temperature of peak 2) for DMAA/MBAM polymer pyrolysis occurred at 399 °C, 401 °C, 405 °C and 411 °C at the heating rates of 2.5, 5, 15 and 20 °C min^{-1}, respectively.

However, both TG and DTG curves presented some differences with an increase in the heating rates. As shown in TG curves, the mass loss of the sample decreased slightly with an increase in the heating rate at a temperature below 420 °C. Here, taking 2.5 °C min^{-1} as an example, approximately

The large mass loss in the temperature range of 200–900 °C correspond to the main pyrolysis stage of the DMAA/MBAM polymer, where large amounts of light gases were given off. Additionally, the thermal degradation of the DMAA/MBAM

Table 2 Degradation temperature of the two peaks in the DTG curves at different heating rates

Heating rate (°C min^{-1})	2.5	5	15	20
Peak 1 (°C)	210	212	220	268
Peak 2 (°C)	399	401	405	411
Height (peak 1) (%/°C)	0.05	0.07	0.15	0.73
Height (peak 2) (%/°C)	0.08	0.28	1.23	1.66
Maximum mass loss (%)	9.79	9.32	8.42	9.21

76.5 wt% polymer in the sample was burnt out, and the mass loss of is approximately 7.5%. But there is no obvious trend of the ultimate maximum mass loss with an increase the heating rate in the temperature range of 420–900 °C. As shown in Table 2, the ultimate mass loss observed at 900 °C for heating rate of 2.5, 5, 15 and 20 °C min^{-1} are 9.79%, 9.32%, 8.42% and 9.21%, respectively. The reasons for this phenomenon might be attributed to the following two points: (1) the sample is more susceptible to cracking at high heating rates, leading to the pyrolysis gas of the polymer to be released more quickly, which may not occur at a lower heating rate. (2) When the heating rates are increased, the partial polymer cannot adequately rapidly pyrolyze and release their volatiles, thereby resulting in hysteresis. Moreover, as seen from Fig. 3, the DTG curves are offset to a high temperature area with an increase in the heating rate, and the degradation temperature was delayed as the heating rate increased. This phenomenon should be due to the fact that more thermal energy was provided for the pyrolysis at the higher heating rate.

The types of gas products and their proportions (in terms of the percentage peak area) during the thermal degradation process of DMAA/MBAM copolymer are identified by Py-GC/MS at different temperatures (240, 385 and 450 °C). The total ion count (TIC) of the main compounds resulting from polymer degradation are presented in Fig. 4 and Table 3. As shown in Fig. 4 and Table 3, the main chemical compositions of the products of gel pyrolysis are the amides and ammonia species with carbon numbers ranging from C_3–C_{12}. Moreover, cyclohexane and cyclohexylamine species, which were the main ring compounds, were mainly detected at 380 °C and 450 °C, whereas ring compounds were scarce at the final pyrolysis temperature of 240 °C. The high temperature leads to a remarkable increase in the characteristic compounds (*N,N*-dimethyl-2-propenamide and trimethylamine, *etc.*) and cyclic compounds (cyclohexane-1,4-*cis*-dicarboxamide and *N*-methyl-n-propyl-cyclohexanamine, *etc.*). When the pyrolysis temperature increases from 240 °C to 450 °C, the relative content of *N,N*-dimethyl-2-propenamide (DMAA monomer) increases from 19.9% to 26.30%, and the relative content of cyclohexane-1,4-*cis*-dicarboxamide can reach 16.98%. This finding is because more energy is provided to the pyrolysis reaction at a higher temperature, which promotes the breakage of carbon chains in

the long chain and the ring opening in the side chain. Therefore, the thermal degradation mechanism of the DMAA/MBAM polymer is mainly divided into two types: depolymerization reactions and random cleavage reactions. The former starts from the chain terminal or weak bonds in the molecule. Once free radical molecules are formed, the C–H and C–O bonds on the adjacent carbon atom are liable to cleavage, thereby causing a chain reaction of monomer loss; the latter is mainly the breakage of the main chain, side groups and end groups occurring inter- or intramolecularly.

4.2 Traditional overall thermal debinding kinetics analysis

The model-free method, also known as the isoconversion method, was used to estimate the thermal debinding kinetics of the DMAA/MBAM polymer for gelcast ceramic parts at heating rates of 2.5, 5, 15 and 20 °C min^{-1}. Fig. 5 illustrates the relationship between E and α (range from 0.025 to 0.975) during the overall debinding process obtained from the FWO, KAS, Friedman and Starink methods. As shown in Fig. 5, the correlation coefficients (R^2) of the linear fits for the four methods are all greater than 0.91 in the conversion range from 0.05–0.7, but the R^2 values are very low in the conversion range below 0.05 and above 0.7. Therefore, the estimated E values at these conversion ranges were inaccurate. This situation may be caused the high heterogeneous characters, which are the comprehensive effects of the secondary or autocatalytic reactions, diffusion, *etc.* Moreover, the changing trend in activation energies obtained by different methods is consistent, but there are obvious fluctuations in values. As the pyrolysis continued, the apparent activation energy in each stage increases at first, then decreases and subsequently increases in the conversion range from 0.05–0.7. The apparent activation energy ranges for the FWO, KAS, Friedman and Starink methods are 221.49–327.56, 222.22–333.27, 121.75–490.08 and 222.47–333.17 kJ mol^{-1}, respectively. The large variation in E indicates that the thermal degradation of DMAA/MBAM copolymer has multiple complex reaction mechanisms during debinding.

It has been shown that the activation energies calculated by the FWO, Starink, Friedman and KAS methods usually differ from each other due to their intrinsic nature.[19,39] The FWO, KAS and Starink methods are based on different approximation algorithms
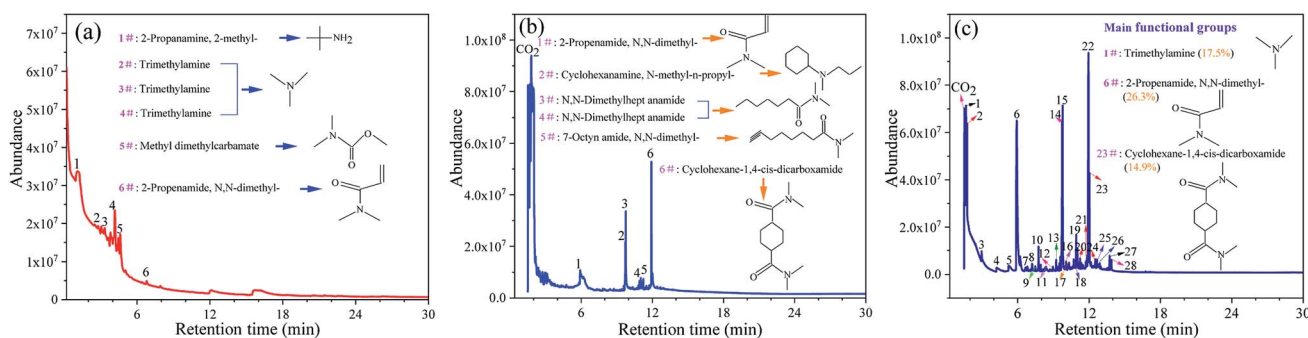

Fig. 4 Details of GC-MS chromatograms with the main identified compounds in the fast pyrolysis of DMAA/MBAM polymer at different final pyrolysis temperatures. (a) 240 °C, (b) 385 °C and (c) 450 °C.

Table 3 The identified compounds in DMAA/MBAM polymer pyrolysis (numbering from Fig. 4c)

No.	Compound	Formula	Molar mass	CAS no.	Relative content/area%
1	Trimethylamine	C_3H_9N	59	75-50-3	17.46
2	2,4-Pentanedia-mine, 2-methyl-	$C_6H_{16}N_2$	116	21586-21-0	7.48
3	2-Propanone, 1-(dimethylamino)-	$C_5H_{11}NO$	101	15364-56-4	0.47
4	Formamide, N,N-dimethyl-	C_3H_7NO	73	68-12-2	1.06
5	Acetamide, N,N-dimethyl-	C_4H_9NO	87	127-19-5	1.86
6	2-Propenamide, N,N-dimethyl-	C_5H_9NO	99	2680-03-7	26.3
7	2,3-Dimethyl-4-hydroxy-2-butenoic lactone	$C_6H_8O_2$	112	1575-46-8	0.48
8	5-Amino-1,3-dimethylpyra-zole	$C_5H_9N_3$	111	3524-32-1	0.69
9	2H-Azepin-2-one, 1,5,6,7-tetrahydro	C_6H_9NO	111	2228-79-7	1.20
10	N,N-Dimethyl cyanoacetamide	$C_5H_8N_2O$	112	7391-40-4	0.41
11	Cyclopentane-cis-1,3-dicarboxamide	$C_7H_{12}N_2O_2$	156	0-00-0	0.31
13	Octanamide, N,N-dimethyl-	$C_{10}H_{21}NO$	171	1118-92-9	1.51
14	Octahydro-2H-pyrido(1,2-a)pyrimidin	$C_8H_{14}N_2O$	154	24025-00-1	6.8
17	4-Cyclopentene-1,3-dione, 4-propyl	$C_8H_{10}O_2$	138	58940-74-2	0.33
18	Cyclohexanecarboxa-mide, N,N-dimethyl-2-oxo-	$C_9H_{15}NO_2$	169	52631-32-0	0.68
21	7-Octynamide, N,N-dimethyl-	$C_{10}H_{17}NO$	167	35066-53-6	0.29
12, 24	Cyclopentane-$trans$-1,3-dicarboxamide	$C_{11}H_{20}N_2O_2$	212	59219-51-1	4.16
15, 19, 20	N,N-Dimethylheptanamide	$C_9H_{19}NO$	157	1115-96-4	11.05
16, 22, 23, 26, 27, 28	Cyclohexane-1,4-cis-dicarboxamide	$C_{12}H_{22}N_2O_2$	226	35541-94-7	16.98

of the temperature integral, which are obtained under the assumption that the activation energy is independent of conversion under isoconversional conditions. Hence, the errors associated with kinetic measurements from the three methods should be dependent on the magnitude of the variation of the activation energy with respect to conversion.[19] Obviously, this situation is not applicable to multistep processes in this study, and a systematic error may be introduced, particularly for the FWO integral method,[40] which is consistent with the solution results in this work. For the Friedman method, it is established without approximation algorithms, but tends to be more sensitive to experimental noise.[41]

4.3 Multipeak fitting result analysis

M-PRM is used to separate the overlapping peaks in dα/dT curves. Fig. 6 gives the fitting results of the subpeaks

Fig. 5 E and R^2 of the pyrolysis of DMAA/MBAM polymer obtained by the FWO, KAS, Friedman and Starink methods.

corresponding to the substages of the debinding process. As shown in Fig. 6a–d, the total thermal debinding process is a weighted composition of the pyrolysis reactions of three pseudocomponents. The three subpeaks exhibit consistent distribution characteristics at different heating rates. Among the three subpeaks, peak 3 has the widest distribution, while peaks 1 and 2 present narrow distributions, indicating that the pyrolysis of pseudo component 3 is the strongest pyrolysis stage. In substage 1, weak bonds (such as C–O, C–N) in the polymer side chains break to form characteristic compounds such as ammonia and amines, as shown in Fig. 4. As the temperature increases, cyclization conditions are generated intramolecularly. In addition to the abovementioned characteristic compounds, cyclic compounds such as cyclohexane and cyclohexylamine are cleaved from the macromolecular chain, and the process includes substage 2. Substage 3 runs through the entire pyrolysis temperature range and possibly includes monomer depolymerization and the carbonization or coking reaction of the molecular chain at the later stage. However, there are some differences in the weighted factors of each subpeak at different heating rates, as tabulated in Table 4. In addition, as the heating rate increases, the temperature range of each subpeak shifts to high-temperature areas, which is related to the delay of pyrolysis of each pseudo component due to inadequate reaction time and heat hysteresis at high heating rates.

To further improve the accuracy of E and k_0, the FWO, KAS, Friedman and Starink methods are applied to estimate the kinetic parameters of each substage analyzed above. Due to space limitations, only the Arrhenius plot of ln(dα/dt) $vs.$ 1/T obtained using Friedman method is illustrated in Fig. 7. Table 5 summarizes the fitting equations and the correlation coefficients (R^2) calculated by the FWO, KAS, Friedman and Starink methods within the conversion range from 0.1–0.9. As shown in Table 5, the R^2 values of almost all the plots are larger than 0.99,
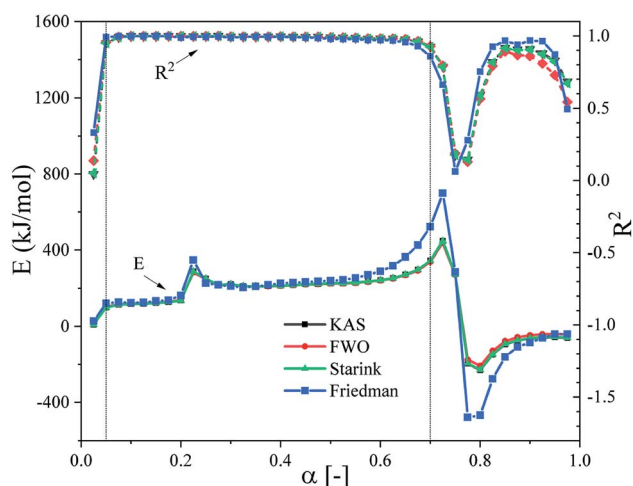
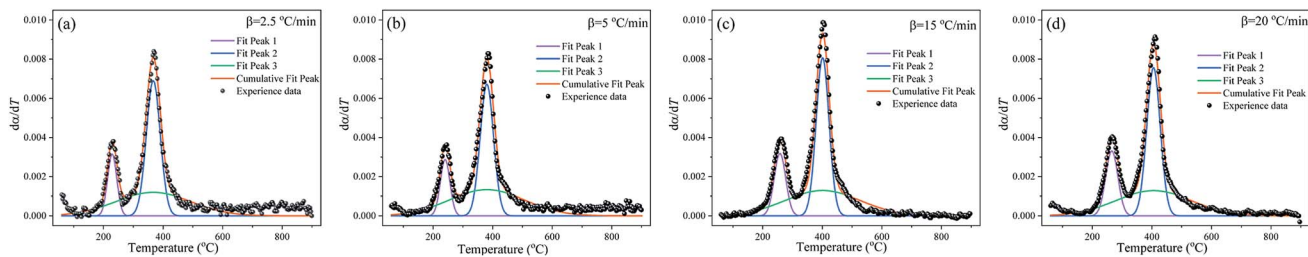**Fig. 6** Gaussian distribution multipeak fitting for the $d\alpha/dT$ curves at different heating rates. (a) 2.5 °C min^{-1}, (b) 5 °C min^{-1}, (c) 15 °C min^{-1} and (d) 20 °C min^{-1}.

Table 4 Weighted factors of each sub-peak at different heating rates in Fig. 6

	Weighted factor (w_i)			
Subpeaks	2.5 °C min^{-1}	5 °C min^{-1}	15 °C min^{-1}	20 °C min^{-1}
Peak 1	0.122	0.116	0.154	0.170
Peak 2	0.404	0.378	0.438	0.430
Peak 3	0.379	0.423	0.409	0.409

reflecting that all four methods can appropriately describe the pyrolysis stage of each subpeak. Compared to the traditional global thermal debinding kinetics analysis, the reliability of the kinetic equations of each subpeak is significantly increased after multipeak fitting.

Fig. 8 shows the E vs. α curves of the three substages estimated via the FWO, KAS, Friedman and Starink methods. As shown in Fig. 8, the variation in the activation energy along with conversion show similar tends for all the four methods. The activation energy values of substages 2 and 3 basically show an increasing trend, while the activation energy values of substage 1 basically shows a decreasing trend, which agrees with the dominant reactants corresponding to the pseudo-components of each substage analyzed above. Moreover, the average values of E showed an increasing tendency from substages 1 to 3. However, there are some difference in the values of activation energy estimated by the four methods. For the FWO, KAS and Starink methods, the apparent activation energy curves of each subpeak substantially overlap for the three methods, and the

difference in the values of E is very small. The values of activation energy calculated by the Friedman method exhibit some differences with other three methods, but the deviations are within acceptable 6% in terms of the average activation energy for each substage. These differences may be attributed to experimental errors and mathematical approximations in the different methods.

Then, the activation energy variable model is used to determine the dependency between the activation energies and conversion for three different subpeaks. Take the differential (Friedman) and the integral (FWO) as examples, for the differential (Friedman) method, the activation energies of substages 1 to 3 are $E(\alpha) = 139.862 - 110.481\alpha + 156.161\alpha^2 - 88.714\alpha^3$ kJ mol^{-1}, $E(\alpha) = 160.791 + 152.496\alpha - 236.906\alpha^2 + 163.724\alpha^3$ kJ mol^{-1} and $E(\alpha) = 72.132 + 452.830\alpha - 669.039\alpha^2 + 507.015\alpha^3$ kJ mol^{-1}, respectively. For the integral (FWO) method, the activation energies of substages 1 to 3 are $E(\alpha) = 152.665 - 123.087\alpha + 182.724\alpha^2 - 103.190\alpha^3$ kJ mol^{-1}, $E(\alpha) = 150.604 + 132.938\alpha - 200.494\alpha^2 + 139.979\alpha^3$ kJ mol^{-1} and $E(\alpha) = 69.668 + 426.576\alpha - 631.607\alpha^2 + 480.782\alpha^3$ kJ mol^{-1}, respectively. Compared with substages 1 and 2, the fluctuation range of the apparent activation energy of substage 3 is larger (113–303 kJ mol^{-1}). This phenomenon indicates that substage 3 may follow a different kinetics mechanism.

Fig. 9 shows the kinetic compensation effect between the apparent activation energy E and the pre-exponential factor k_0 (obtained by the Friedman method) of each substage separated by an M-PRM. It can be seen from Fig. 9 that the R^2 of plots of E and $\ln(k_0)$ for each subpeak are relatively high, indicating that
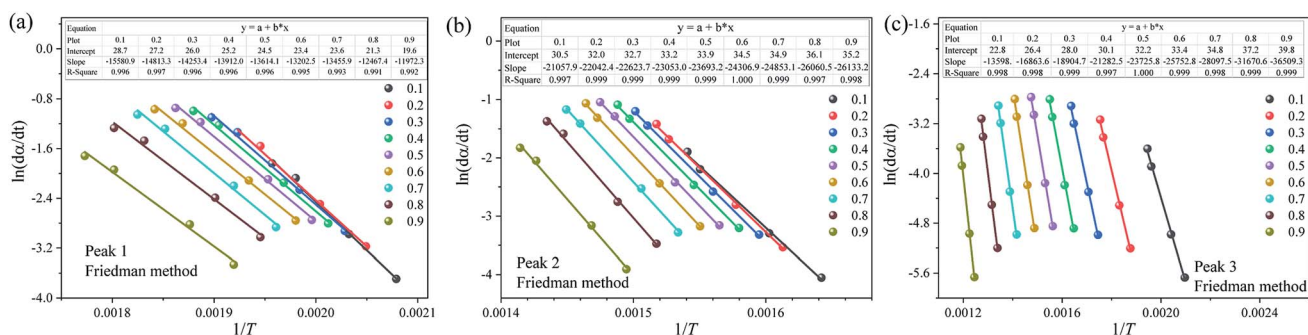

Fig. 7 Arrhenius plot of $\ln(d\alpha/dt)$ vs. $1/T$ of each pyrolysis stage at different conversion rates using the Friedman method. (a) Peak 1, (b) peak 2 and (c) peak 3.

Table 5   Kinetic equations for each pyrolysis stage by the FWO, KAS, Friedman and Starink methods

Sub-peaks	α	KAS method Slope	Intercept	R^2	FWO method Slope	Intercept	R^2	Starink method Slope	Intercept	R^2	Friedman method Slope	Intercept	R^2
Peak 1	0.1	−16 657.40	23.16	0.993	−17 648.70	37.57	0.994	−16 756.53	24.60	0.993	−15 580.92	28.71	0.996
	0.2	−15 901.33	21.10	0.997	−16 908.74	35.54	0.997	−16 002.08	22.54	0.997	−14 813.31	27.19	0.997
	0.3	−15 291.93	19.53	0.996	−16 311.24	34.00	0.997	−15 393.86	20.98	0.996	−14 253.36	26.01	0.996
	0.4	−15 014.45	18.71	0.997	−16 042.78	33.20	0.998	−15 117.28	20.16	0.997	−13 912.01	25.21	0.996
	0.5	−14 752.28	17.94	0.998	−15 789.63	32.45	0.998	−14 856.02	19.39	0.998	−13 614.14	24.46	0.996
	0.6	−14 345.37	16.88	0.996	−15 392.51	31.40	0.996	−14 450.08	18.33	0.996	−13 202.48	23.41	0.995
	0.7	−14 486.00	16.88	0.996	−15 543.23	31.42	0.996	−14 591.73	18.33	0.996	−13 455.88	23.57	0.993
	0.8	−13 703.20	15.12	0.995	−14 771.23	29.68	0.996	−13 810.00	16.57	0.995	−12 467.41	21.27	0.991
	0.9	−13 294.38	13.96	0.996	−14 378.41	28.55	0.996	−13 402.78	15.42	0.996	−11 972.30	19.57	0.992
Peak 2	0.1	−19 158.87	19.51	0.996	−20 416.92	34.40	0.996	−19 284.67	21.00	0.996	−21 057.91	30.49	0.997
	0.2	−20 308.29	20.78	0.997	−21 587.44	35.70	0.998	−20 436.21	22.27	0.997	−22 042.44	32.00	0.999
	0.3	−20 769.69	21.13	0.997	−22 062.84	36.07	0.998	−20 899.00	22.62	0.997	−22 623.69	32.74	0.999
	0.4	−21 169.29	21.43	0.997	−22 474.45	36.39	0.998	−21 299.80	22.92	0.997	−23 053.01	33.20	0.999
	0.5	−21 863.64	22.18	0.998	−23 180.47	37.16	0.998	−21 995.32	23.68	0.998	−23 693.16	33.90	0.999
	0.6	−22 475.86	22.81	0.998	−23 804.10	37.81	0.999	−22 608.69	24.31	0.998	−24 306.88	34.51	1.000
	0.7	−23 074.89	23.35	1.000	−24 416.91	38.37	1.000	−23 209.09	24.85	1.000	−24 853.11	34.87	0.999
	0.8	−24 092.11	24.47	0.999	−25 447.76	39.51	0.999	−24 227.67	25.98	0.999	−26 060.51	36.06	0.997
	0.9	−24 610.47	24.70	1.000	−25 986.23	39.76	1.000	−24 748.04	26.20	1.000	−26 133.22	35.18	0.998
Peak 3	0.1	−12 675.85	15.13	0.998	−13 666.77	29.54	0.998	−12 774.94	16.57	0.998	−13 598.24	22.81	0.998
	0.2	−15 830.03	18.03	0.998	−16 933.06	32.66	0.998	−15 940.34	19.50	0.998	−16 863.61	26.41	0.998
	0.3	−17 736.18	19.15	0.998	−18 920.33	33.92	0.998	−17 854.60	20.63	0.998	−18 904.71	27.98	0.999
	0.4	−20 058.95	21.11	0.997	−21 311.00	35.99	0.997	−20 184.16	22.59	0.997	−21 282.46	30.14	0.997
	0.5	−22 435.54	23.03	0.999	−23 753.44	38.01	0.999	−22 567.33	24.53	0.999	−23 725.80	32.20	1.000
	0.6	−24 397.50	24.19	0.998	−25 779.77	39.26	0.999	−24 535.73	25.69	0.998	−25 752.78	33.43	0.999
	0.7	−26 689.84	25.57	0.998	−28 140.74	40.74	0.999	−26 834.93	27.09	0.998	−28 097.48	34.78	0.998
	0.8	−30 148.25	28.03	0.999	−31 680.58	43.31	0.999	−30 301.48	29.56	0.999	−31 670.58	37.18	0.999
	0.9	−34 838.05	30.91	0.999	−36 482.43	46.33	0.999	−35 002.49	32.45	0.999	−36 509.31	39.79	0.999

the E and k_0 of each substage exhibit a kinetic compensation effect.

4.4 Determination of the most appropriate mechanism function $f(\alpha)$

To further determine the kinetic mechanism of the removal of DMAA/MBAM polymer from gelcast ceramic parts, the mechanism function of the thermal debinding stages is determined by Málek's procedure.[32] The results of the experimental and theoretical master plots depicted in Fig. 10 demonstrate the most appropriate mechanism function for each substage at different heating rates. It can be seen from Fig. 10 that the substages corresponding to the pyrolysis process of the pseudocomponents do not follow a single-process reaction mechanism. At different heating rates, each substage can be divided into two zones with $\alpha = 0.5$ in the experimental plots as the boundary. The first and second substages follow the same kinetics mechanism, and the most appropriate mechanism function for the pyrolysis processes of pseudo components 1 and 2 are the reaction-order model (F_2) in the conversion range of $0 < \alpha < 0.5$; however, the most appropriate mechanism function changes to the 3D Zhuravlev–Lesokhin–Tempelman mechanism model (D-
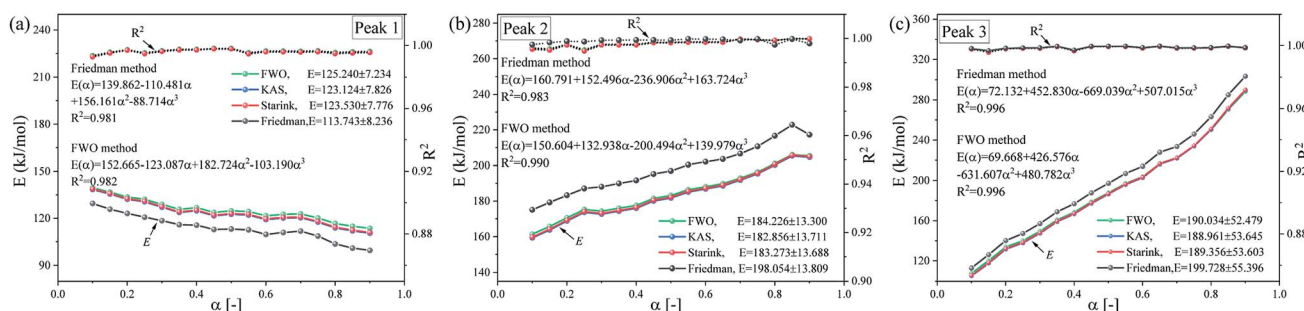

Fig. 8 The dependence of E on the degree of α for subpeaks in the entire debinding process using the FWO, KAS, Friedman and Starink methods. (a) Peak 1, (b) peak 2 and (c) peak 3.
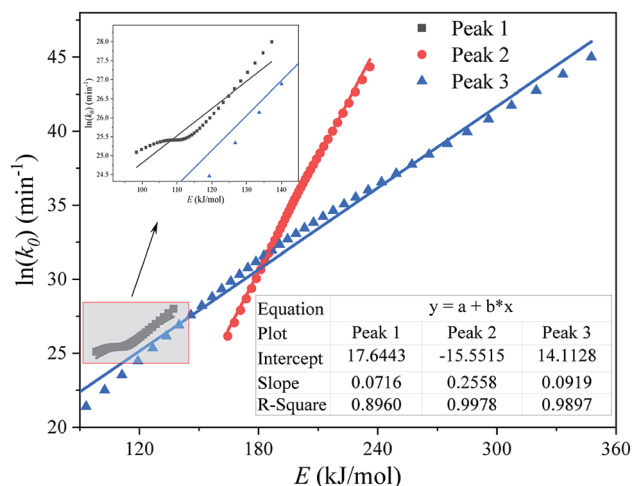
Fig. 9 Plot of $\ln(k_0)$ vs. E (calculated by the Friedman method) for each substage of the pyrolysis process of the DMAA/MBAM polymer during the debinding process.

Table 6 The optimum SB model parameters for the three substages

Parameter		Peak 1	Peak 2	Peak 3
Weighted factor	w_i	0.149	0.439	0.412
SB	n	0.668	0.700	1.049
	m	3.049	3.177	−0.161
	p	−3.874	−3.962	0.518
Differential (Friedman)				
$\ln(k(\alpha))$	p_1	28.309	25.174	18.920
	p_2	−13.087	40.646	53.097
	p_3	19.766	−60.199	−76.419
	p_4	−9.978	39.651	50.662
$E(\alpha)$	p_5	139.862	160.791	72.132
	p_6	−110.481	152.496	452.830
	p_7	156.161	−236.906	−669.039
	p_8	−88.714	163.724	507.015
Integral (FWO)				
$\ln(k(\alpha))$	p_1	31.389	23.217	18.124
	p_2	−16.678	37.640	49.514
	p_3	26.793	−54.330	−71.448
	p_4	−13.923	35.869	47.801
$E(\alpha)$	p_5	152.665	150.604	69.668
	p_6	−123.087	132.938	426.576
	p_7	182.724	−200.494	−631.607
	p_8	−103.190	139.979	480.782

ZLT_3) in the conversion range of $0.5 < \alpha < 1$. For the third substage, the kinetic mechanism of the pyrolysis process of pseudo component 3 is well fit by a 3D Diffusion-Jander model (D-J_3) ($0 < \alpha < 0.5$) and an Avrami–Erofeev model (A_4) ($0.5 < \alpha < 1$) mechanism model.

Furthermore, the SB model is applied to determine the mechanism function of the complex debinding processes for the three substages at different heating rates.[32,37] Using the $E(\alpha)$ and k_0 obtained from the differential Friedman and integral (FWO) methods, the optimized parameters (n, m, p) for SB model are summarized in Table 6, and the fitting results of the SB model are depicted in Fig. 11. It can be seen from Fig. 11, the R^2 values of the nonlinear regression fitting equation for each subpeak are all greater 0.99, indicating that the SB model can interpret the thermal degradation mechanism of DMAA/MBAM polymer. The reaction mechanism of the DMAA/MBAM pyrolysis is complex, which is the combined effects of the reaction order, power law, and diffusion mechanisms. The reaction mechanisms for substages 1 to 3 are $f(\alpha) = (1 - \alpha)^{0.668}\alpha^{3.049}(-\ln(1 - \alpha))^{-3.874}$, $f(\alpha) = (1 - \alpha)^{0.700}\alpha^{3.177}(-\ln(1 - \alpha))^{-3.962}$ and $f(\alpha) = (1 - \alpha)^{1.049}\alpha^{-0.161}(-\ln(1 - \alpha))^{0.518}$, respectively.

Therefore, the kinetic mechanism does not change at different heating rates. A high heating rate may complicate the

pyrolysis reaction process (shown in Fig. 4), but has almost no effect on the reaction mechanism. This effect is because the pyrolysis reaction of each substage is controlled by the dominant reactants, that is, the three pseudo-components, when the pyrolysis is stable, which also reveals the thermal stability and inherent reactivity of the DMAA/MBAM polymer.

4.5 Model prediction

The comparison between the experimental and SB model predicted α and $d\alpha/dT$ curves of the pyrolysis process of the DMAA/MBAM polymer over the whole degradation run at a heating rate of 10 °C min⁻¹ is shown in Fig. 12. It can be seen from Fig. 12 that the α and $d\alpha/dT$ curves predicted by integral (FWO) and differential (Friedman) model-fit basically overlap, which indicates that the two methods have similar accuracy with respect to the SB model. It is also found that the SB model predicted values are very close to the experimental α and $d\alpha/dT$ values, except at lower (<0.05) and higher (>0.95) conversions. This
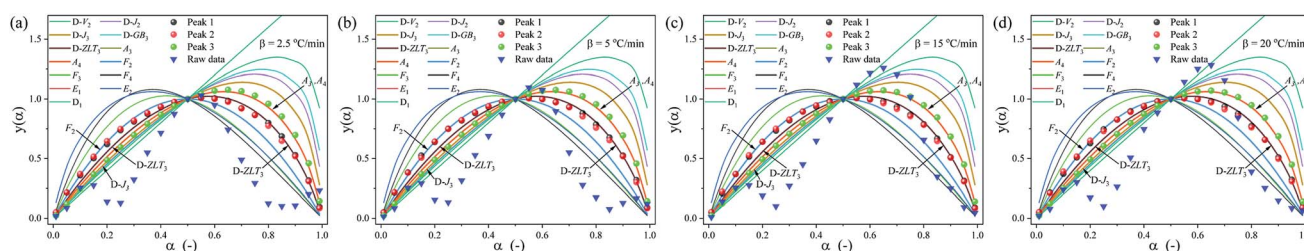

Fig. 10 Standard $y(\alpha)$ and experimentally derived master plots against different α values at different heating rates. (a) 2.5 °C min⁻¹, (b) 5 °C min⁻¹, (c) 15 °C min⁻¹ and (d) 20 °C min⁻¹.
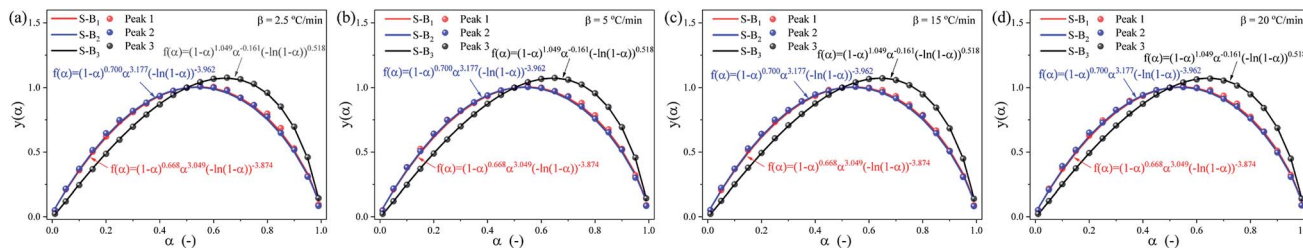
Fig. 11 SB model $y(\alpha)$ and experimentally derived master plots against different α values at different heating rates. (a) 2.5 °C min^{-1}, (b) 5 °C min^{-1}, (c) 15 °C min^{-1} and (d) 20 °C min^{-1}.
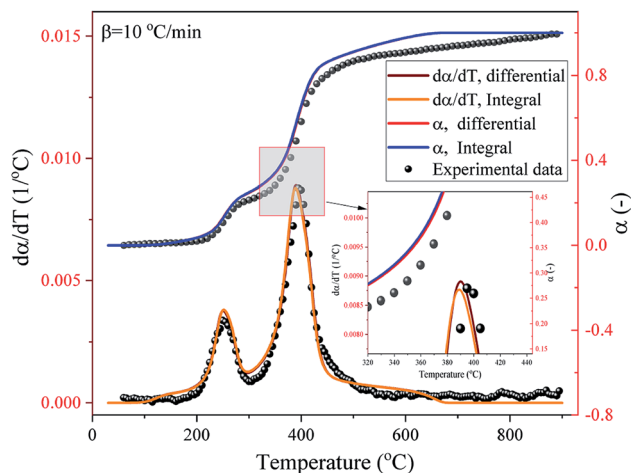

Fig. 12 Experimental and SB model predicted α and $d\alpha/dT$ curves of the pyrolysis process of the DMAA/MBAM polymer at a heating rate of 10 °C min^{-1}.

deviation may be due to the complex multiple reactions that occur throughout the active pyrolysis process. The predicted values are in good agreement with the experimental values and the maximum error is less than 9%, which indicates that the SB model can be used for the prediction of the thermal degradation course over the whole degradation run.

5 Conclusions

This work investigated the thermal degradation characteristics of DMAA/MBAM copolymer through TG and Py-GC/MS experiments. M-PRM was proposed to separate the overlapping peaks in the $d\alpha/dT$ curves. The kinetic parameters (E, k_0) of each substage were calculated using the FWO, KAS, Friedman and Starink methods. In addition, the reaction mechanism of each substage was analyzed and discussed by Málek's procedure and the SB model. The main conclusions are as follows:

(1) TG analysis showed that the dehydration stage occurs at temperatures below 200 °C, and the thermal degradation of the DMAA/MBAM copolymer mainly occurs in two temperature ranges: 200–300 °C and 300–600 °C. Py-GC/MS analysis showed that the relevant monomers of copolymerization and the characteristic compounds generated from gel pyrolysis are primarily amides and ammonia species. Moreover, cyclohexane and

cyclohexylamine species, which were the main ring compounds, were mainly detected at 385 °C and 450 °C, whereas ring compounds were scarce at the final pyrolysis temperature of 240 °C.

(2) A three-stage parallel reaction model was able to accurately describe the thermal debinding behavior and multiplex reaction mechanisms of removing DMAA/MBAM polymer from gelcast ceramic parts. The activation energies of substages 1 to 3 calculated by the Friedman method and activation energy variable model are $E(\alpha) = 139.862 - 110.481\alpha + 156.161\alpha^2 - 88.714\alpha^3$ kJ mol^{-1}, $E(\alpha) = 160.791 + 152.496\alpha - 236.906\alpha^2 + 163.724\alpha^3$ kJ mol^{-1} and $E(\alpha) = 72.132 + 452.830\alpha - 669.039\alpha^2 + 507.015\alpha^3$ kJ mol^{-1}, respectively. The average values of E showed an increasing trend from substages 1 to 3, and a kinetic compensation effect was also found between the E and k_0 of each substage.

(3) The kinetic mechanism determined by SB model revealed that the reaction mechanism for substages 1 to 3 are $f(\alpha) = (1 - \alpha)^{0.668}\alpha^{3.049}(-\ln(1 - \alpha))^{-3.874}$, $f(\alpha) = (1 - \alpha)^{0.700}\alpha^{3.177}(-\ln(1 - \alpha))^{-3.962}$ and $f(\alpha) = (1 - \alpha)^{1.049}\alpha^{-0.161}(-\ln(1 - \alpha))^{0.518}$, respectively. The α and $d\alpha/dT$ curves predicted by SB model were in good agreement with the experimental values, indicating that the SB model was an effective tool for the prediction of the thermal degradation course of DMAA/MBAM copolymer during the whole debinding process.

Conflicts of interest

The authors declare that they have no conflict of interest.

Acknowledgements

Notes and references

1 T. Deng, Y. Wang, A. Dufresne and N. Lin, *Carbohydr. Polym.*, 2018, **181**, 111–118.

2 S. Yin, L. Pan, L. Guo, Y. Liu, Y. Feng, T. Qiu and J. Yang, *Ceram. Int.*, 2018, **44**, 7569–7579.

3 L. Montanaro, B. Coppola, P. Palmero and J.-M. Tulliani, *Ceram. Int.*, 2019, **45**, 9653–9673.

4 P. Jamshidi, N. Lu, G. Liu, E. Herny and M. M. Attallah, *Ceram. Int.*, 2018, **44**, 3440–3447.

5 B. Paulina and S. Mikolaj, *J. Therm. Anal. Calorim.*, 2012, **109**, 773–782.

6 G. Chen, P. Cao, G. Wen and N. Edmonds, *Mater. Chem. Phys.*, 2013, **139**, 557–565.

7 G. Fu, N. Loh, S. Tor, B. Tay, Y. Murakoshi and R. Maeda, *Appl. Phys. A: Mater. Sci. Process.*, 2005, **81**, 495–500.

8 W.-W. Yang, K.-Y. Yang, M.-C. Wang and M.-H. Hon, *Ceram. Int.*, 2003, **29**, 745–756.

9 R. K. Enneti, T. S. Shivashankar, S.-J. Park, R. M. German and S. V. Atre, *Powder Technol.*, 2012, **228**, 14–17.

10 L. Liu, N. Loh, B. Tay, S. Tor, Y. Murakoshi and R. Maeda, *Mater. Lett.*, 2007, **61**, 809–812.

11 S. M. Ani, A. Muchtar, N. Muhamad and J. A. Ghani, *Ceram. Int.*, 2014, **40**, 2819–2824.

12 L. Gorjan, A. Dakskobler and T. Kosmač, *J. Am. Ceram. Soc.*, 2012, **95**, 188–193.

13 J. Xue, M. Dong, J. Li, G. Zhou and S. Wang, *J. Am. Ceram. Soc.*, 2010, **93**, 928–930.

14 H. Yuan, C. Jia, X. Zhang, K. Bekouche and Z. Wang, *Chinese Journal of Engineering*, 2016, **38**, 102–107.

15 L. Zhang, L. Zhang, L. Wang, H. Zhou, P. Liu, Z. Li and Y. Huang, *Rare Met. Mater. Eng.*, 2008, **37**, 697–701.

16 S. J. Lombardo, *J. Am. Ceram. Soc.*, 2015, **98**, 57–65.

17 Z. Shi, Z. Guo and J. Song, *Acta Mater.*, 2002, **50**, 1937–1950.

18 M. Belgacem, B. Thierry and G. Jean-Claude, *Powder Technol.*, 2013, **235**, 192–202.

19 M. Salehi, F. Clemens, T. Graule and B. Grobéty, *Appl. Energy*, 2012, **95**, 147–155.

20 M. Hu, Z. Chen, S. Wang, D. Guo, C. Ma, Y. Zhou, J. Chen, M. Laghari, S. Fazal, B. Xiao, B. Zhang and S. Ma, *Energy Convers. Manage.*, 2016, **118**, 1–11.

21 C. Zhang, T. Qiu, J. Yang and J. Guo, *Mater. Sci. Eng., A*, 2012, **539**, 243–249.

22 H.-X. Xu, T. Qiu, J. Yang and J. Guo, *J. Inorg. Mater.*, 2011, **26**, 1105–1110.

23 W. Wan, C. e Huang, J. Yang, J. Zeng and T. Qiu, *J. Electron. Mater.*, 2014, **43**, 2566–2572.

24 J. Tong and D. Chen, *Ceram. Int.*, 2004, **30**, 2061–2066.

25 L. Shen, X. Xu, W. Lu and B. Shi, *Ceram. Int.*, 2016, **42**, 5569–5574.

26 J. Guo, T. Qiu, J. Yang, Y. Feng, C. Zhang, W. Zhang and T. Guo, *Ceram. Int.*, 2012, **38**, 2905–2911.

27 J. Li, C. Zhang, R. Yin and W. Zhang, *Ceram. Int.*, 2019, **45**, 8166–8174.

28 J. Li, C. Zhang, R. Yin and W. Zhang, *RSC Adv.*, 2019, **9**, 8415–8425.

29 Y. Q. Li, T. Qiu and J. Xu, *Mater. Res. Bull.*, 1997, **32**, 1173–1179.

30 A. S. Khan, Z. Man, M. A. Bustam, C. F. Kait, Z. Ullah, A. Nasrullah, M. I. Khan, G. Gonfa, P. Ahmad and N. Muhammad, *J. Mol. Liq.*, 2016, **223**, 754–762.

31 J. H. Flynn, *Thermochim. Acta*, 1997, **300**, 83–92.

32 Y. Sun, F. Bai, X. Lü, C. Jia, Q. Wang, M. Guo, Q. Li and W. Guo, *Energy*, 2015, **82**, 705–713.

33 M. Starink, *Thermochim. Acta*, 1996, **288**, 97–104.

34 C. Xie, J. Liu, X. Zhang, W. Xie, J. Sun, K. Chang, J. Kuo, W. Xie, C. Liu, S. Sun, M. Buyukada and F. Evrendilek, *Appl. Energy*, 2018, **212**, 786–795.

35 G. Sun, H. Sun, Y. Liu, B. Zhao, N. Zhu and K. Hu, *Polymer*, 2007, **48**, 330–337.

36 I. Ali, H. Bahaitham and R. Naebulharam, *Bioresour. Technol.*, 2017, **235**, 1–11.

37 P. Šimon, *Thermochim. Acta*, 2011, **520**, 156–157.

38 J. Šesták and G. Berggren, *Thermochim. Acta*, 1971, **3**, 1–12.

39 S. Vyazovkin and C. A. Wight, *Thermochim. Acta*, 1999, **340–341**, 53–68.

40 S. Vyazovkin, A. K. Burnham, J. M. Criado, L. A. Pérez-Maqueda, C. Popescu and N. Sbirrazzuoli, *Thermochim. Acta*, 2011, **520**, 1–19.

41 P. Budrugeac, *Polym. Degrad. Stab.*, 2001, **74**, 125–132.